

# Bio-inspired Flow Sensing and Control: Autonomous Rheotaxis Using Distributed Pressure Measurements

Francis D Lagor, Levi D DeVries, Kathryn M Waychoff, Derek A Paley  
Department of Aerospace Engineering, University of Maryland, USA

**Abstract**—This paper presents the design and use of an artificial lateral-line system for a bio-inspired robotic fish capable of autonomous flow-speed estimation and rheotaxis (the natural tendency of fish to orient upstream), using only flow-sensing information. We first present a feedback controller based on the difference between pressure measurements collected on opposite sides of the fish robot. We then describe a dynamic rheotaxis controller based on a potential-flow model and a Bayesian observer that uses two or more pressure sensors in an arbitrary arrangement. Pressure sensor placements are selected based on nonlinear observability analysis. Experimental results demonstrate the advantages of the proposed scheme, which include robustness to model error and sensor noise. The primary contribution of this paper is a framework for rheotaxis and flow-speed estimation based on pressure-difference information that does not require fitting model parameters to flow field conditions.

**Keywords**—autonomous rheotaxis, flow sensing and control, pressure sensing, artificial lateral line.

## I. INTRODUCTION

One challenging consideration for mobile autonomous robotic systems is the influence of an unknown or unsteady flow field [19], [11], [23]. However, a flow field provides rich information to the evolutionarily adaptive, flow-sensing features present in some biological systems [6], [24]. The field of bio-inspired flow-sensing has developed with the following objectives: (1) to use biological structures to inform the design, fabrication, and packaging of artificial flow-sensing devices for autonomous robotics [11], [27]; and (2) to develop algorithms for data assimilation and control that use these complex flow-sensing arrays to achieve specific functional goals, such as local flow field estimation, object identification, and navigation [1], [13], [23].

One prominent example of an advanced biological flow-sensing system is the lateral-line system present in all cartilaginous and bony fish and aquatic amphibians [13], [24]. The uses of the lateral-line system in fish behavior include orienting in flow (rheotaxis), schooling, detecting obstacles, and avoiding predators. For example, the blind Mexican cave fish (*Astyanax fasciatus*) relies exclusively on the lateral-line system for orienting, navigating, and schooling [24], [6]. The lateral-line system runs the length of the fish and is made up of receptors, known as neuromasts, ranging in number from under 100 to over 1000 [24]. The neuromasts consist of ciliary bundles of hair cells,

covered in a gelatinous outer dome called a cupula, that serve as mechano-electrical transducers with directional sensitivity [6]. Neuromasts exist in two types: superficial neuromasts, which are located on the exterior surface; and canal neuromasts, which are located between pore entrances of a subdermal lateral-line canal. Superficial neuromasts serve as flow-velocity sensors, whereas canal neuromasts respond to pressure-driven flow in the canal in order to measure pressure differences [25].

Two specific fish behaviors of interest for bio-inspired robotics are rheotaxis and station-holding, because they serve as foundational behaviors from which one can construct a more complex repertoire. Rheotaxis is a behavior in which a fish orients upstream toward oncoming flow [17]; station-holding is a behavior in which a fish maintains position behind an upstream obstacle [6]. The lateral-line sensing modalities are thought to play an important role in executing these behaviors [6]. An artificial lateral-line system for use on an autonomous underwater vehicle would enhance its autonomy by providing a short-range sensing modality. Moreover, it would provide indispensable sensory information in dark, murky, or cluttered environments, where traditional sensing modalities like vision or sonar may be impaired.

Since the first artificial lateral-line was fabricated [26], researchers have developed artificial lateral-line systems using a variety of sensor types, including microfabricated hot-wire anemometry [26], capacitive [8], piezoresistive [28], optical [13], and ionic polymer metal composite cantilever [1] sensors. Yang *et al.* [27] designed an artificial lateral-line canal and demonstrated the properties of band-pass filtering and noise rejection in dipolar and turbulent flows. Tao and Yu [24] provided a comprehensive review of biomimetic hair flow sensors, and Ren and Mosheni [20] performed analytical work for flow sensing of a Kármán vortex street. Abdulsadda and Tan [1] created an artificial lateral-line using ionic polymer metal composite cantilever sensors and trained an artificial neural network to localize a dipole source. Venturelli *et al.* [25] showed that an artificial lateral-line made of off-the-shelf piezoresistive pressure sensors (approximating pressure-difference measurements of canal neuromasts) can be used to identify the presence of a Kármán vortex street and its hydrodynamic features. Kottapalli *et al.* [15], [14] developed liquid crystal polymer pressure sensors in a flexible array for mounting on curved surfaces. Asadnia *et al.* [3] produced a piezoelectric artificial lateral-line requiring zero power input.

Although many investigators have constructed artificial lateral-line systems, few have implemented closed-loop

estimation and control using sensor data, and these controllers have been empirical in nature. For example, Salumäe *et al.* [23] demonstrated closed-loop rheotaxis of a fish robot using pressure sensors and a Braitenberg controller, which is a memoryless controller that uses direct pressure readings from sensors on opposing sides of the fish to turn in the direction of increasing signal strength. Using empirical techniques, Salumäe and Kruusmaa [22] also demonstrated closed-loop station-holding control of a fish robot. Work is still needed to develop model-based controllers in a robust control framework that will be extensible to more complex flow environments.

This paper describes the principled design and implementation of a dynamic control framework for rheotaxis of a bio-inspired fish robot that includes model-based estimation of flow field parameters using two or more pressure sensors in an arbitrary arrangement. The technical approach employs a reduced-order fluid-mechanical model for flow past a streamlined body based on potential-flow theory. We select sensor locations that maximize nonlinear observability of the flow field parameters. We utilize a recursive Bayesian filter to estimate the flow speed and angle-of-attack. To validate the potential-flow model, we perform computational fluid dynamic (CFD) simulations and laboratory experiments. Finally, we experimentally test our rheotaxis controllers in a testbed consisting of a 185L flow tank, a two-degree-of-freedom mechanical gantry system, and a fish robot endowed with commercially-available pressure sensors.

The technical approach is justified by the following rationale: potential-flow theory produces a reduced-order model with few parameters that can be used within a real-time control loop; recursive Bayesian filtering can handle nonlinear observation operators (without linearization) and arbitrary non-Gaussian probability densities; and a simple proportional control law permits easier assessment of the filter performance in the control loop.

The contributions of this paper are (1) the design and fabrication of a robotic testbed for bio-inspired flow estimation and control algorithms; (2) the demonstration of closed-loop rheotaxis behavior using two pressure sensors and a proportional controller; (3) Bayesian estimation of angle-of-attack and flow speed; and (4) the use of the estimated angle-of-attack in a dynamic rheotaxis controller for a fish robot with two or more pressure sensors in a possibly asymmetric configuration. The contributions represent the first experimental implementation of model-based rheotaxis control of a fish robot based on pressure-difference measurements without first training an empirical or fluid-mechanical model to match the flow field conditions.

The outline of the paper is as follows. Section II describes a potential-flow model for flow past a fish robot and a measurement equation for pressure differences in an artificial lateral line. Section III discusses the experimental testbed and compares the potential-flow model to CFD simulation and laboratory experiments. Section IV presents analysis of flow observability using distributed pressure sensors. Section V gives an overview of recursive Bayesian filtering and presents the framework for dynamic feedback control. Section VI describes results from fixed angle-of-attack and flow speed estimation, rheotaxis based on pressure-difference feedback control, and the

Bayesian dynamic rheotaxis controller. Section VII summarizes the paper and ongoing research.

## II. PRESSURE DIFFERENCE SENSOR MODEL

This section presents a reduced-order fluid-mechanics model for flow past a fish body and a measurement equation to predict pressure differences between sensor locations in a bio-inspired artificial lateral-line.

### A. Flow past a streamlined body

In order to make estimates of flow parameters based on sensor measurements, we invoke an idealized model of fluid flow past a streamlined airfoil. We employ potential-flow theory and conformal mapping, making use of the Joukowski transformation [18], [2]. Let  $\xi = Re^{i\theta} + \lambda$ , where  $\theta \in [0, 2\pi)$ , be a disk of radius  $R$  centered at  $\lambda$ , and let  $b = R - |\lambda|$  [18]. Using the complex plane to represent a two-dimensional domain, the transformation [18]

$$z = \xi + \frac{b^2}{\xi} \quad (1)$$

maps a disk into a symmetric streamlined body centered at the origin [18]. Let  $U > 0$  be the free-stream flow speed and  $\alpha$  be the angle-of-attack of the fish relative to the flow (when viewed from above). When transformation (1) is used in conjunction with the following complex potential [2], [18]

$$w(\xi) = U(\xi - \lambda)e^{-i\alpha} + \frac{R^2}{\xi - \lambda}Ue^{i\alpha} + 2iRU\sin(\alpha)\ln(\xi - \lambda) \quad (2)$$

it maps uniform flow past a cylindrical disk into uniform flow past a streamlined body [18], [9]. The first term in the complex potential (2) represents the uniform flow, the second term introduces the boundary condition, and the third term enforces the Kutta condition, which states that the rear stagnation point must occur at the trailing tip of the airfoil.

The conjugate flow  $f^*(z)$  around the body in  $z$  coordinates is [18], [9]

$$f^*(z) = \left( Ue^{-i\alpha} - \frac{R^2}{(\xi(z) - \lambda)^2}Ue^{i\alpha} + \frac{2iRU\sin\alpha}{(\xi(z) - \lambda)} \right) \left( 1 - \frac{b^2}{(\xi(z))^2} \right)^{-1} \quad (3)$$

where  $\xi(z)$  is the dual-valued inverse mapping of (1) with values selected to lie outside of the fish body [18], [9], i.e.,

$$\xi(z) = \begin{cases} \frac{1}{2}(z + \sqrt{z^2 - 4b^2}) & \text{if } \arg(z) \in \left(-\frac{\pi}{2}, \frac{\pi}{2}\right) \\ \frac{1}{2}(z - \sqrt{z^2 - 4b^2}) & \text{if } \arg(z) \in \left(\frac{\pi}{2}, \frac{3\pi}{2}\right) \end{cases} \quad (4)$$

The real and imaginary parts of  $f(z)$  give the components of the flow field. Note that the flow is evaluated at sensor locations and is parameterized by the free-stream flow speed  $U$  and angle-of-attack  $\alpha$ .

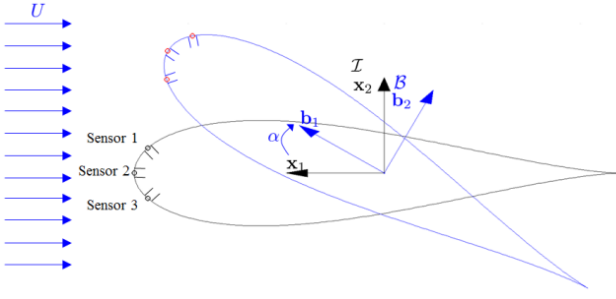


Figure 1 Relevant reference frames and flow field parameters describing a one-degree-of-freedom robotic fish (top view)

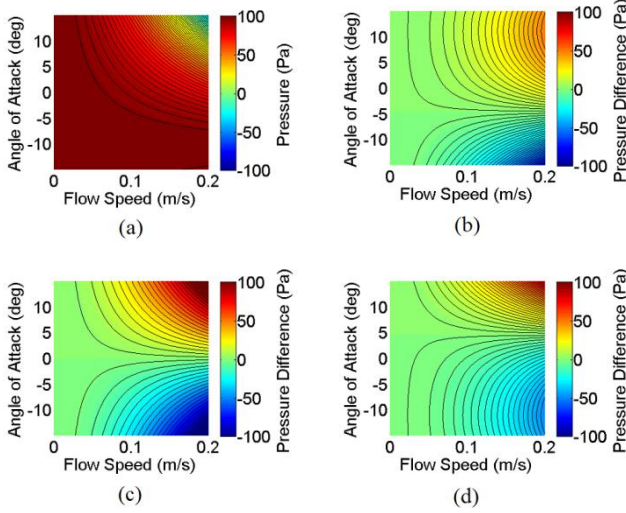


Figure 2 (a) Fluid pressure at the  $p_1$  sensor location; (b) pressure difference between  $p_1, p_2$ ; (c)  $p_1, p_3$ ; and (d)  $p_2, p_3$  sensors locations

### B. Pressure measurement equation

Consider multiple pressure sensors distributed around the body of a fish robot enclosed within canals as shown in **Figure 1**, with  $p_i$  denoting the pressure at sensor location  $i$ . A model of the pressure values predicted by the potential-flow model (3) is obtained from Bernoulli's principle for inviscid, incompressible flow along a streamline [10], i.e.,

$$\frac{v^2}{2} + gz + \frac{p}{\rho} = C, \quad (5)$$

where  $v$  is the local flow speed,  $g$  is the acceleration of gravity,  $z$  is the elevation,  $p$  is the static pressure,  $\rho$  is the fluid density, and  $C$  is a constant describing the total specific energy of a fluid parcel moving along the streamline. Applying (5) to two equal-elevation locations along a streamline, one of which is a stagnation point, results in the following expression for pressure  $p$  in terms of the streamline's stagnation pressure  $p_s$  [10]:

$$\frac{v_1^2}{2} + \frac{p_1}{\rho} = \frac{p_s}{\rho},$$

which implies (after dropping the subscript)

$$p = p_s - \rho \frac{v^2}{2}.$$

**Figure 2a** shows the pressure  $p$  for various flow field parameters with stagnation pressure  $p_s = 100$  Pa.

For an unknown angle-of-attack, the stagnation pressure  $p_s$  is not known. However, the difference between two pressure sensors is

$$\Delta p_{12} = p_2 - p_1 = \frac{\rho}{2}(v_1^2 - v_2^2).$$

Hence, a measurement equation based on the pressure difference offers the advantage that the stagnation pressure, an identifying characteristic of the flow condition, does not need to be known *a priori*. The measurement function for the case of three sensors is a vector collecting individual pressure differences  $\Delta p = [\Delta p_{12}, \Delta p_{13}, \Delta p_{23}]^T$ , where  $\Delta p_{ij}$  indicates the pressure difference from sensor  $i$  to sensor  $j$ . **Figures 2b, c, and d** illustrate pressure difference values between sensor pairs available in **Figure 1** for various flow conditions. The maximum value of  $U = 0.2$  m/s corresponds to a flow speed of 2 body lengths per second for a 10 cm fish. We plot only angles-of-attack  $\alpha \in [-15^\circ, 15^\circ]$ , since the flow model is accurate only for small angles due to the stall condition that arises in the study of airfoils [2], [9]. Nonetheless, in experiments described in this paper, we allow evaluation of the model in the range  $\alpha \in [-35^\circ, 35^\circ]$ .

Assume that the pressure measurements contain additive Gaussian white noise, i.e., the  $i$ th sensor measurement is

$$\tilde{p}_i = p_i + \eta_i, \quad (6)$$

where  $\eta_i$  has a zero-mean Gaussian distribution with  $\sigma_i^2$  variance,  $\mathcal{N}_i(0, \sigma_i^2)$ . (Note, the difference between sensor signals produce another random variable,  $\eta_j - \eta_i$ , which has distribution  $\mathcal{N}(0, \sigma_i^2 + \sigma_j^2)$ ). Let  $\Omega = [U, \alpha]^T$ . The measurement equation, after substitution of the flow model (3) and inclusion of the measurement noise model (6), becomes

$$\Delta \tilde{p}_{ij}(z_i, z_j; \Omega) = \frac{\rho}{2} (|f^*(z_i, \Omega)|^2 - |f^*(z_j, \Omega)|^2) + \eta_j - \eta_i. \quad (7)$$

The pressure difference in (7) may be based on sensors arbitrarily distributed around the fish body; equation (7) does not require that the pressure sensors be close together. Thus, (7) is a bio-inspired, but not bio-mimetic, approach to pressure sensing, since pressure differences measured by canal neuromasts in the lateral-line result from the fluid pressure at neighboring pore locations [20]. Equation (7) can be used to estimate  $\Omega$  from pressure measurements. However, **Figure 2c** shows that  $U$  is unobservable at zero angle-of-attack for the symmetric  $p_1, p_3$  sensor pair, because all flow speeds give  $\Delta p_{13} = 0$ . **Figures 2b** and **2d** show how this unobservable region shifts in parameter space for asymmetric sensor pairs. Similarly,  $\alpha$  is unobservable if  $U$  is zero. Observability is also lost if the pressure difference is smaller than the noise level of the sensors. The observability properties for pressure-difference flow-sensing arrays are discussed further in Section IV.

### III. ROBOTIC TESTBED FOR FLOW-SENSING AND CONTROL

This section describes the laboratory testbed constructed for experimental validation of the flow-sensing and control framework and presents an evaluation of the potential-flow

model using computational fluid dynamics (CFD) simulations and the experimental testbed.

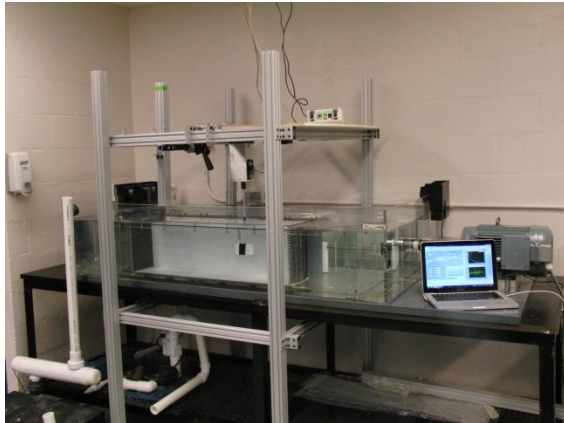


**Figure 3** The laboratory testbed consists of a 185 L flowtank and a two-degree-of-freedom underwater robot equipped with commercially available pressure sensors. The motors that regulate the robot position and orientation are controlled by a laptop computer

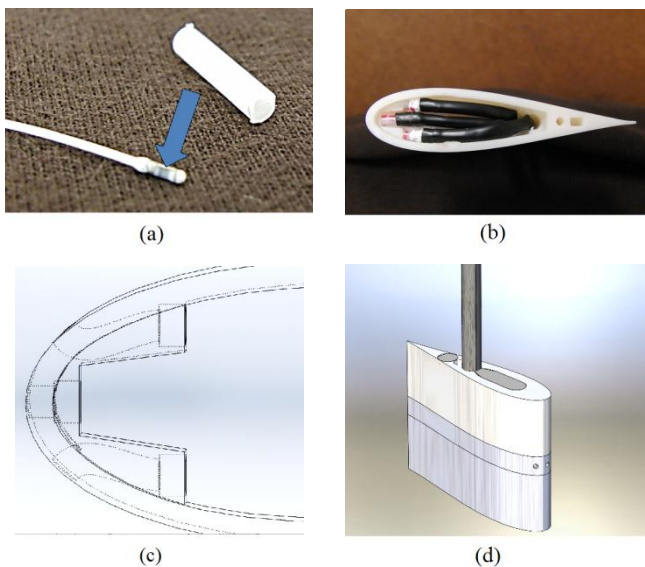


**Figure 4** Images of fish robot used in the experiments: (a) Mikro-Tip pressure sensor (arrow points to rectangular sensing area on side of the device tip) and Delrin isolation tube; (b) sensors installed in fish within Delrin tubes and PTFE sleeving; (c) internal canal features of the fish robot; (d) CAD image of assembled robot

#### A. Flow-sensing and control experimental setup

**Figure 3** shows the laboratory testbed, which consists of a 185 L flowtank (Loligo Systems, SW10275 modified) and a two-degree-of-freedom custom robot equipped with commercially available pressure sensors (Millar Instruments, Mikro-Tip Catheter Pressure Transducers, model SPR-524). The flow tank has a flow straightener and a 25 x 25 x 87.5 cm enclosed test section. A 5 x 22 cm slot in the top of the test section provides access for the robotic control arm. Calibration of the flow tank is accomplished using a Hach FH950 portable flow meter. A mechanical gantry system provides overhead control of the robot's orientation and cross-stream position (although only orientation control is used in this paper). The

gantry is elevated by a custom support fixture (materials from 80/20, Inc.) and consists of an LS-100-18-H linear lead screw table (Anaheim Automation), coupled to a secondary stepper motor for rotary motion. Both stepper motors are STM23Q-XAE integrated stepper drives (Applied Motion Products), which take commands from LabVIEW via an RS-232 serial connection. The drives contain built-in motion controllers that accept high-level text commands, most notably feed-to-length and jog commands for control of motor position or angular velocity. The stepper motors also contain integrated encoders that are queried directly from LabVIEW. Each fish robot is constructed from a 3D-printed airfoil shape when viewed from above, as shown in **Figure 4**. Choosing  $R = 2.9$  cm and  $\lambda = -0.5$  cm yields a 9.9 cm by 2.2 cm by 6 cm fish that approximately resembles the length and width characteristics of a Mottled sculpin (*Cottus baridi*) [4], [21], a fish previously studied for rheotactic response [7]. The height of the fish robot (6 cm) reduces the three-dimensional effects of the flow near sensor locations. The fish is printed on a uPrint SEPlus printer (Stratasys Ltd) in three pieces with a hollow inner pocket and port holes with small canals for the sensors. **Figure 1** shows the locations of the three pressure sensors used in these experiments. Sensor placement is based on the observability analysis described in Section IV. The sensors are piezoresistive pressure transducers with a straight end (size 3.5F), containing a small rectangular sensing region on the side of the device tip, as shown in **Figure 4a**. The sensors connect to two PCU-2000 Pressure Control Units (Millar Instruments) and are embedded in canals to shield from direct impingement of the fluid flow. The sensors read the static pressure, which enables analysis using the potential-flow model as described in Section II. The sensors are secured in small Delrin tubes within the fish robot using Teflon tape (see **Figures 4a** and **4b**). Calibration of each sensor is performed by submersion in a known hydrostatic pressure; all sensors in this work have calibration constants within 1% of the manufacturer-supplied value of 13.30 kPa/V. Soaking the sensors in water for 30 minutes prior to use reduces sensor drift. Further, pressure data is collected in still water; after each run, we verify that sensor drift has not exceeded 2%, similar to Venturelli *et al.* [25]. A NI-USB-6225 data acquisition board, with a BNC-2115 connector block (National Instruments) provides the link between the pressure sensors and the LabVIEW software interface. Sampling occurs at 1000 Hz (within the frequency response limits of the pressure sensors). However, using the mean of 200 samples as an individual measurement increases the signal-to-noise ratio; thus, the effective sampling rate for data collection is 5 Hz. The control loop frequency for all rheotaxis experiments is set to 1 Hz to account for differences in computation time between the control schemes.

**Figure 5** shows a time-averaged cross-stream pressure survey of the flow tank. It reveals periodic structures approximately 6 cm wide that align with the guide vanes located upstream of the flow straightener. The fluid mechanical model presented in Section II does not account for such variations. Although autonomous navigation in a spatially varying flow field is the subject of ongoing work, we reduced these variations by

including additional flow straightening structures. Adding two pieces of 3.5 cm wide, 3 mm pore size honeycomb (Nomex) and an additional flow straightener (Loligo Systems) with 7 cm spacing between each component reduces the cross-stream pressure variations as shown in the **Figure 5**. Note that, although

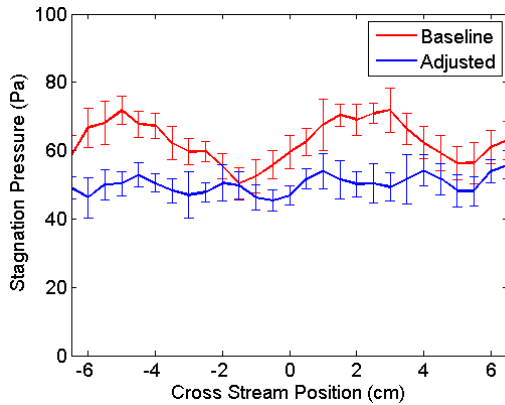


**Figure 5** Cross-stream pressure survey (zero is channel center) of the Loligo 185L flowtank, before and after modification.  $U = 0.26$  m/s (both curves).

the standard deviation (error bars) may increase at a given location, the overall maximum, minimum, and average standard deviations are reduced. **Figure 6b** illustrates the arrangement of the additional honeycomb in the swim channel.

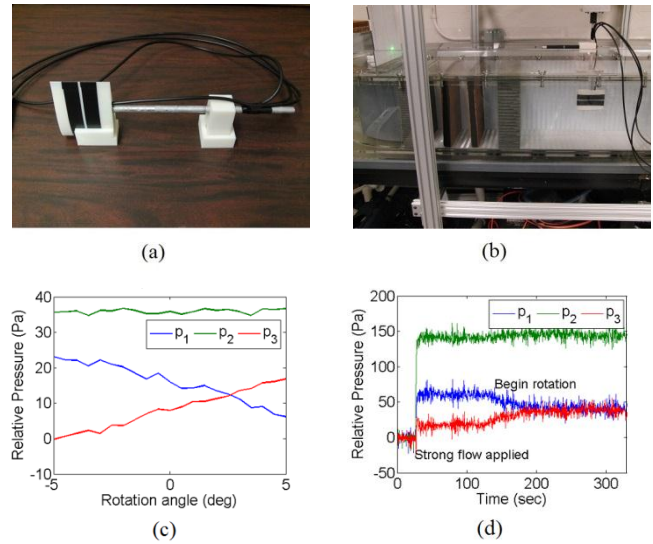


**Figure 6** Initial fish alignment. (a) Custom 3D-printed tools for aligning the fish body and holder for a laser pointer; (b) Alignment of the fish robot using laser; (c) Time-averaged relative pressures ( $U = .22$ m/s) during a rotary scan after laser alignment; (d) Final alignment: equalizing  $p_1, p_3$  pressures.

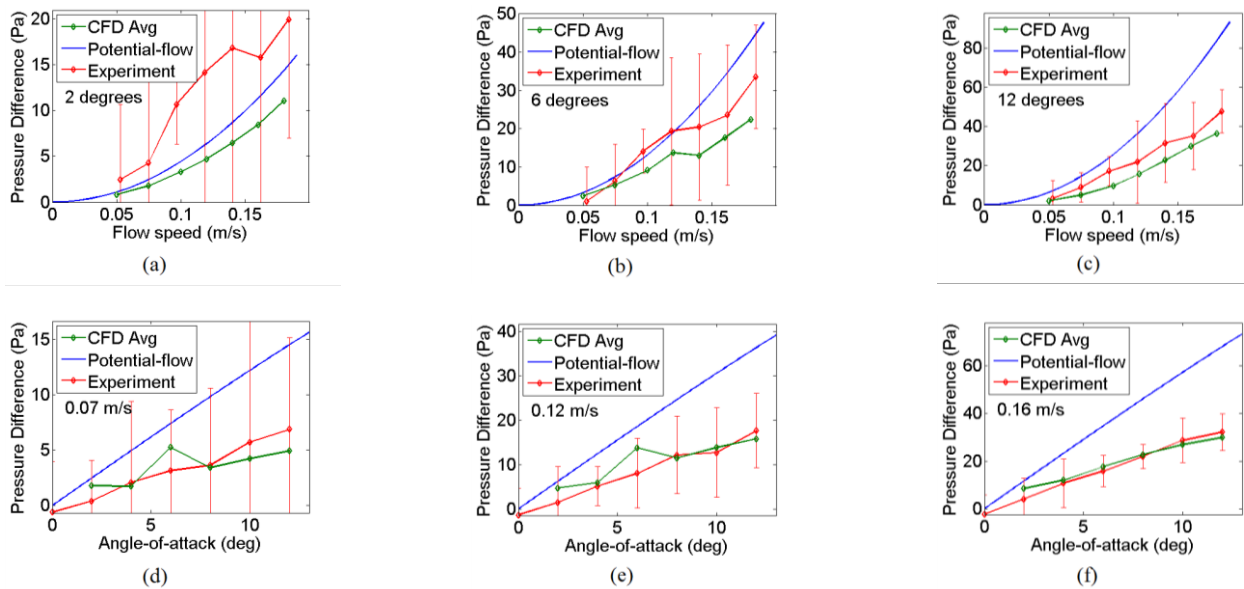


**Figure 7** Evaluation of the potential-flow model using CFD and experiments. (a), (b), and (c) Comparisons for constant angle-of-attack; (d), (e), and (f) comparisons for constant flow speed. Error bars represent the standard deviation of the experimental data.

Since the encoder in the rotary gantry motor provides only a relative rotational measurement, an initial alignment procedure is necessary. The fish body is first aligned to a holder for a laser pointer using 3D-printed tooling (see **Figure 6a**); next, the fish is rotated until the laser illuminates markings corresponding to the center of the test section (see **Figure 6b**). After this procedure, we perform a rotary sweep ( $\pm 5^\circ$ ) collecting

time-averaged pressure measurements. **Figure 6c** illustrates the time-averaged pressure measurements collected during a  $\pm 5^\circ$  rotary sweep of the fish. Note that the  $p_2$  signal is relatively flat and the  $p_1, p_3$  signals cross at a location of equal pressure. Due to the symmetric placement of the sensors, the crossing of the  $p_1, p_3$  signals at a location away from the zero orientation indicates an error that can be attributed to the manufacturing

tolerances of the flow tank and the 3D-printed fish, uncertainties in the laser alignment process, and variations in the pressure field. To define the upstream zero orientation (zero angle-of-attack), we rotate the fish robot in a strong flow ( $U = .47\text{m/s}$ ) until the  $p_1, p_3$  pressures are equal. **Figure 6d** shows the pressure signals during this process. We note that the final alignment does not visually differ from the laser aligned condition, i.e., it is accurate to within  $3^\circ$  of the upstream direction.

### B. Potential-flow model evaluation

To validate the potential-flow model from Section II, we compare it with simulations from a commercially available CFD solver (COMSOL) and experimental sensor data. The COMSOL CFD simulations solve the Reynolds Averaged Navier Stokes equations with a Spalart-Allmaras turbulence model [5]. **Figures 7a, 7b,** and **7c** show the pressure difference  $\Delta p_{13}$  for constant angles-of-attack. **Figures 7d, 7e,** and **7f** show the pressure difference  $\Delta p_{13}$  for constant flow speeds. For low flow speeds and angles-of-attack, the potential-flow model accurately represents the physical phenomenon captured in the high-fidelity CFD model, with decreasing accuracy at higher speeds and angles. (We note that a small difference exists in the inlet boundary condition for the CFD simulations and experiments; the CFD inlet boundary condition is the free stream flow speed measured by the flow probe at the location occupied by the fish during testing, not the true flow speed of the inlet to the test section).

Discrepancies with experimental data are likely due to sensor noise, angular alignment uncertainty, disturbances in the free-stream flow, cross-stream flow non-uniformities, and unmodelled viscous effects. **Figure 8** shows the onset of flow separation from the fish body, a viscous effect captured by the CFD simulations. When flow separation occurs, the streamlines of the flow no longer conform to the shape of the streamlined body, due to a region of backflow or recirculating flow on the upper surface of the fish, often leading to an unsteady, turbulent wake [18]. The potential-flow pressure-difference model of Section II assumes that the flow is steady, irrotational, inviscid, and conforms to the body of the fish. Further, the flow conditions considered in this paper (0.05 m/s to 0.20 m/s) have free-stream Reynolds numbers that range from 12,500 to 50,000 in the test section. These values exceed the 2,300 demarcation value for transition from laminar to turbulent flow that is often used for internal flows [10], clearly violating the laminar flow assumption of the potential-flow model. Nonetheless, the potential-flow model still proves useful in a control loop, because it captures the general shape of the pertinent physical relationships. Note that the accuracy of the potential-flow model increases as the angle-of-attack approaches zero. The potential-flow model is also a reduced-order model, offering the possibility of real-time implementation.

## IV. OPTIMIZING SENSOR PLACEMENT FOR FLOW OBSERVABILITY

This section describes the optimal sensor placement, based on maximizing the observability of unknown flow parameters.

### A. Nonlinear observability

In dynamical systems theory, the presence of a full-rank condition in the observability gramian indicates that the state of a system can be inferred from observations of the output [16]. However, for a nonlinear system, the observability gramian may not be easily formed through linearization about an equilibrium point [9], [16]. The empirical observability gramian  $W_o \in \mathbb{R}^{N \times N}$ , where  $N$  is the number of estimated parameters, provides a local, central-difference-based approximation to the observability gramian that requires only evaluations of the nonlinear measurement function for perturbed state conditions. The  $(i, j)$ th component of  $W_o$  is [9], [16]

$$W_o(i, j) = \frac{1}{4\varepsilon_i \varepsilon_j} \int_0^T [\mathbf{y}^{+i}(\tau) - \mathbf{y}^{-i}(\tau)]^T \times [\mathbf{y}^{+j}(\tau) - \mathbf{y}^{-j}(\tau)] d\tau, \quad (8)$$

$$i = 1, \dots, N, \quad j = 1, \dots, N,$$

where  $\mathbf{y}^{\pm i}$  is the perturbed output corresponding to the perturbed state  $\mathbf{x}^{\pm i} = \mathbf{x} \pm \varepsilon_i \mathbf{e}_i$ . If the system fails to satisfy the observability rank condition in any open subset of the state space, then the system is not locally observable [16]. If, however, the observability rank condition holds, the reciprocal of the smallest local singular value,  $\mu \triangleq 1/\sigma_{\min}$ , provides a measure of how difficult it is to estimate the state from the measurements of the system output [16], [9]. The quantity  $\mu$  is often referred to as the local unobservability index [16]. In the following, we use the unobservability index as a measure for choosing optimal sensor placements, similar to [9].

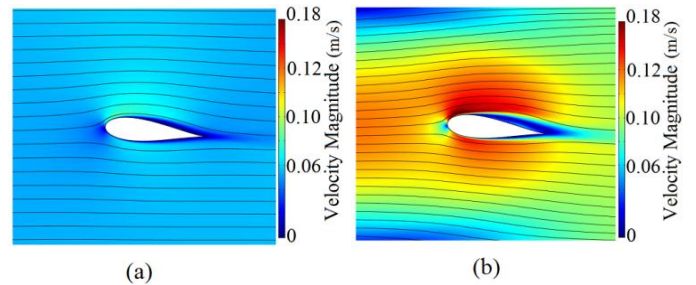


**Figure 8** CFD simulations showing the onset of flow separation. (a)  $6^\circ$  angle-of-attack,  $U = 0.05$  m/s; (b)  $6^\circ$  angle-of-attack,  $U = 0.14$  m/s

### B. Optimal sensor placement

Numerical calculation of the empirical observability gramian for a sensor pair at a constant angle-of-attack reveals that the joint state  $(U, \alpha)$  is not locally observable, regardless of the pair placement, because  $W_o \in \mathbb{R}^{2 \times 2}$  has rank one. However, observability may be restored if one combines measurements from the same sensor pair at different angles (i.e., if the fish robot is permitted to move). Further, observability can be restored for either the  $U$  or  $\alpha$  parameter-estimation problem if an estimate of the accompanying state component is known (e.g., via another sensing modality). **Figure 9** shows the results for optimizing placement of a pair of pressure sensors to observe a fixed angle-of-attack for several discrete angles. Although the flow speed must be known, the results are independent of its actual value [9].

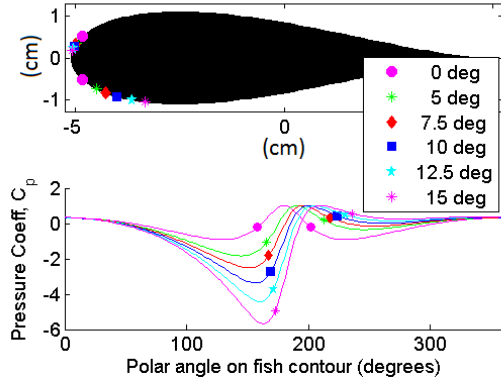


**Figure 9** Optimal placement locations for a pair of pressure sensors based on observability of several discrete angles-of-attack.

**Figure 9** plots the nondimensional coefficient of pressure [18]  $C_p \triangleq 1 - v^2/U^2$  versus polar angle around the fish body, starting from  $0^\circ$  at the tail, wrapping counter-clockwise to  $180^\circ$  at the nose, and returning to  $360^\circ$  at the tail. Whenever the flow velocity on the surface of the fish body is zero, the flow is stagnant and the pressure is maximum, so  $C_p = 1$ . Note that the sensor pairs always straddle the stagnation point, as seen in the lower subplot. Further, for increasing angles-of-attack, one of the sensor locations approaches the nose of the fish. Performing this analysis for angles in the range of  $\alpha = [-15^\circ, 15^\circ]$  in increments of  $2.5^\circ$  and summing the observability gramian values over all angles, we find that the optimal sensor pair for zero angle-of-attack is also the optimal pair for observing arbitrary angles-of-attack.

Optimization of the nonlinear observability in the three-sensor case produces an asymmetric result, with a corresponding mirror configuration (mirrored about the real axis) that is also optimal. In the experimental work, we use three sensors in a symmetric layout; two pressure sensors are at the optimal two-sensors locations and a third sensor is at the nose of the fish. The joint state  $(U, \alpha)$  is observable with this three-sensor configuration, and its symmetry allows for proper flow field alignment. Furthermore, as shown experimentally in Section VI, ignoring the signal from the nose sensor, leaves a two sensor configuration that is optimal for observing angle-of-attack.

## V. ESTIMATION AND CONTROL FRAMEWORK FOR RHEOTAXIS

This section describes an approximate recursive Bayesian filter for estimating flow field parameters from pressure measurements and a dynamic control framework for rheotaxis.

### A. Bayesian estimation and filtering

Bayesian estimation is a technique by which knowledge of an unknown quantity is enhanced through the assimilation of measurements [12]. Bayes' formula is [12]

$$\underbrace{\pi(x|y)}_{\text{posterior}} \propto \underbrace{\pi(y|x)}_{\text{likelihood}} \underbrace{\pi(x)}_{\text{prior}}, \quad (9)$$

where  $\pi(\cdot)$  represents a probability density function (pdf). The central idea is to use Bayes' formula (9) to adjust the prior

understanding of an unknown quantity  $x$ , represented in the form of a pdf, based upon the likelihood that a measurement  $y$  was generated by a nearby state of the system. Normalization of the posterior density is required to ensure the total integral of the pdf sums to unity. (The  $\propto$  symbol is used to indicate a proportional relationship). In practice, we perform grid-based Bayesian estimation, in which a finite volume of parameter space is discretized, and the pdf's are approximated on this grid. Normalization is performed by dividing the weight at each grid point by the total weight, summed over all grid points. The assumption of additive Gaussian measurement noise results in a Gaussian likelihood function

$$\pi(\Delta\tilde{p}|\mathbf{z}, \boldsymbol{\Omega}) \propto \exp\left(-\frac{1}{2}(\Delta\tilde{p} - \Delta p(\mathbf{z}, \boldsymbol{\Omega}))^T \Sigma^{-1}(\Delta\tilde{p} - \Delta p(\mathbf{z}, \boldsymbol{\Omega}))\right)$$

where  $\Sigma$  is the measurement covariance matrix. For the three-sensor case,  $\Sigma = \text{diag}(\sigma_1^2 + \sigma_2^2, \sigma_1^2 + \sigma_3^2, \sigma_2^2 + \sigma_3^2)$ , otherwise  $\Sigma = (\sigma_i^2 + \sigma_j^2)$  for a single  $p_i, p_j$  sensor pair. (The variances are chosen by collecting data from the pressure sensors and analyzing the noise statistics. Since the noise in the sensor measurements increases with free-stream flow speed, we choose the values based on measurements at the maximum relevant flow speed.)

Pressure sensors provide a sequence of measurements represented by  $\mathbf{D}(t - \Delta t) \triangleq \{\Delta\tilde{p}(t - \Delta t), \dots, \Delta\tilde{p}(t_0)\}$ . The posterior probability density from the previous  $t - \Delta t$  assimilation time is used as the prior density for assimilation at time  $t$ , yielding

$$\pi(\boldsymbol{\Omega}(t)|\mathbf{D}(t)) \propto \pi(\Delta\tilde{p}(t)|\boldsymbol{\Omega}(t))\pi(\boldsymbol{\Omega}(t - \Delta t)|\mathbf{D}(t - \Delta t)) \quad (10)$$

The state evolution equation and the measurement equation together are an evolution-observation model, for which our knowledge of the system state can evolve in time and be augmented with new information through the following sequential, recursive scheme, known as Bayesian filtering [12]:

- Time evolution of the pdf (prediction) is accomplished using the Chapman-Kolmogorov equation [12]

$$\begin{aligned} & \pi(\boldsymbol{\Omega}(t + \Delta t)|D(t)) \\ &= \int \pi(\boldsymbol{\Omega}(t + \Delta t)|\boldsymbol{\Omega}(t)) \pi(\boldsymbol{\Omega}(t)|D(t)) d\boldsymbol{\Omega}(t) \end{aligned} \quad (11)$$

- Assimilation of the observations occurs via Bayes' formula [12]

$$\begin{aligned} & \pi(\boldsymbol{\Omega}(t + \Delta t)|D(t + \Delta t)) \\ & \propto \pi(D(t + \Delta t)|\boldsymbol{\Omega}(t + \Delta t))\pi(\boldsymbol{\Omega}(t + \Delta t)|D(t)). \end{aligned} \quad (12)$$

We choose  $\pi(\boldsymbol{\Omega}(t + \Delta t)|\boldsymbol{\Omega}(t))$  to be a Gaussian transition density, with variance tuned to maximize estimator/filter performance.

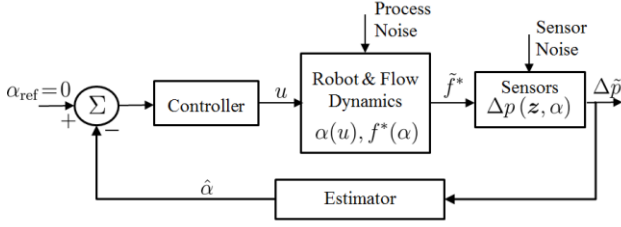


Figure 10 Flow sensing, estimation and control framework for rheotaxis

### B. Dynamic control design

We now present a model-based dynamic controller for rheotaxis for which a block diagram is shown in **Figure 10**. The kinematics of the robot turning at a commanded angular rate  $u$  are

$$\dot{\alpha} = u, \quad (13)$$

where  $u$  is the control input. The Bayesian filter produces estimates of  $\hat{\alpha}$  and  $\hat{U}$  as the robot moves. The estimate  $\hat{\Omega}(t)$  is the maximum *a posteriori* estimate of (12), i.e.,

$$\hat{\Omega}(t) \triangleq \underset{\Omega}{\operatorname{argmax}} \pi(\Omega(t)|D(t)) \quad (14)$$

The controller calculates the control input with the proportional control law [9]

$$u = -K_1 \hat{\alpha}.$$

Note that if  $\hat{\alpha} = 0$ , then the closed-loop system  $\dot{\alpha} = -K_1 \hat{\alpha}$  is in equilibrium. Moreover, if the filter produces  $\hat{\alpha}$  estimates that at least have the correct sign as the true orientation, then the robot will drive toward  $\alpha = 0$ , which is the direction of increasing model validity. We have shown previously that, if the estimation error is bounded, then the angle-of-attack error is uniformly, ultimately bounded, with ultimate bound inversely proportional to the control gain  $K$  [9]; this result is illustrated by the experimental results of Section VI. Since the Bayesian filter is applied in real-time, it is necessary to account for the fish motion during the estimation step. Let (11) serve as the evolution equation with process uncertainty so that the prior pdf for the next Bayesian assimilation cycle represents the best estimate of the system state. The transition density is [9]

$$\pi(\Omega(t + \Delta t)|\Omega(t)) = N(\Psi, \Sigma_{pr}),$$

where  $\Psi \triangleq [0 \ \Delta t \dot{\alpha}(t)]^T$ .

## VI. EXPERIMENTAL DEMONSTRATION OF RHEOTAXIS CONTROL

This section presents estimation results for angle-of-attack and flow speed using the potential-flow model and a Bayesian filter, assuming the true values are constant. It also includes results of a rheotaxis controller based on pressure-difference feedback control, and it compares these results to the performance of dynamic rheotaxis control based on recursive Bayesian filtering.

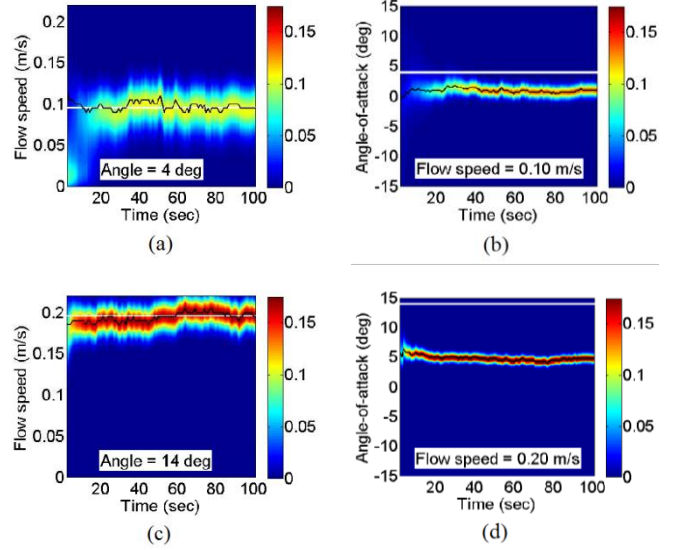


Figure 11 Estimation results for fixed angle-of-attack and flow speed. Contour plots show the marginal pdf's at each instant in time. The estimate (mode) is shown in black, and the white lines indicate the ground truth values.

### A. Constant angle-of-attack and flow speed estimation

Results of Bayesian estimation for constant angles-of-attack and flow speed experiments are shown in **Figure 11**. **Figures 11a** and **11b** present the marginal pdf's and estimated parameter values (based on the mode of the joint posterior density) for an angle-of-attack of  $4^\circ$  and a fixed flow speed of 0.10 m/s. **Figure 11c** and **11d** illustrate the case of an angle-of-attack of  $14^\circ$  and a fixed flow speed of 0.20 m/s. These two cases span a large portion of the desired operational range and are representative of the results in most configurations. In both cases, the Bayesian estimator provides a reasonable flow-speed estimate within only a few seconds. The flow speed estimates are accurate throughout the remainder of the run. However, in all cases, the estimator systematically underestimates the angle-of-attack. Nonetheless, after properly tuning the observer gains, the angle-of-attack estimate always tends towards a steady value with the correct sign, similar to **Figures 11b** and **11d**. We attribute the filter's inability to estimate angle-of-attack to model errors. Note in the model comparison results of **Figure 7** that the model fit to experimental results for flowspeed at a constant angle-of-attack is superior to the model fit for angle-of-attack.

### B. Rheotaxis via pressure-difference feedback control

We first implement a feedback control for rheotaxis based directly on the  $\Delta p_{13}$  pressure difference from the  $p_1, p_3$  pressure sensors located on opposing sides of the fish robot (see **Figure 1**). The control input  $u$  is calculated according to the proportional control law

$$u = -K_2 \Delta \tilde{p}_{13} \quad (15)$$

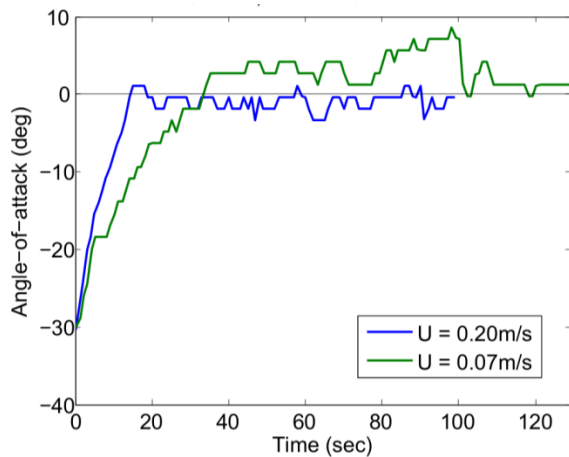


Figure 12 Results of robotic rheotaxis using a pressure-difference feedback control.

where  $K_2$  is a proportional gain. Figure 12 shows the results of the rheotaxis experiment using (15) for two separate flow speeds. Note that convergence to the desired orientation is not monotonic. Further, 20 to 40 seconds elapse before rheotaxis is achieved, and the convergence rate and variations in orientation are dependent on flow speed. It is evident that the pressure-difference signal is jagged and noisy. Although the proportional control law (15) is sufficient to accomplish rheotaxis, it lacks memory of past measurements, causing sensitivity to sensor noise, and also requires sensors to be symmetrically arranged on the fish.

C. Rheotaxis via dynamic control with Bayesian filtering

Figure 13 presents results from rheotaxis experiments using the estimation and control framework and the  $[\Delta p_{12}, \Delta p_{13}, \Delta p_{23}]^T$  measurement signals from the sensor

arrangement in Figure 1. Figures 13a, b, and c show an experiment with a flow speed of 0.12 m/s and an initial angle-of-attack of 30°. Figures 13d, e, and f present another experiment with a flow speed of 0.07 m/s and an initial angle-of-attack of -30°. Although the Bayesian filter typically underestimates the angle-of-attack as shown in the constant angle-of-attack estimation, in both cases the control loop drives the fish robot to the correct upstream direction, because the estimation error vanishes at zero angle-of-attack. These results show that a dynamic controller based on the potential-flow model achieves rheotaxis from an uncertain initial orientation outside the accurate domain of the potential-flow model.

Although the Bayesian estimation approach increases the computational work required, one of its benefits over simple pressure difference control is reduced long-term sensitivity to sensor noise. Figure 13 shows the estimator transient response is short ( $< 20s$ ). Although the estimator exhibits sensitivity to noise in the transient period, it maintains its final estimates without large excursions due to noisy data. This benefit is due in part to the filter’s ability to assimilate  $\Delta p$  measurements from multiple sensor pairs. The 0.07 m/s case was selected for direct comparison to the performance of the simple pressure difference controller under the same conditons. The low flow-speed condition is challenging for both controllers due to the low pressure signal-to-noise ratio. The time history of the Bayesian controller results in a steady, long-term orientation of the robot. Note in Figure 13d the estimator initially generates an angle-of-attack estimate with the wrong sign, causing the robot to turn in the wrong direction, before correcting the filter estimate and driving to zero angle-of-attack.

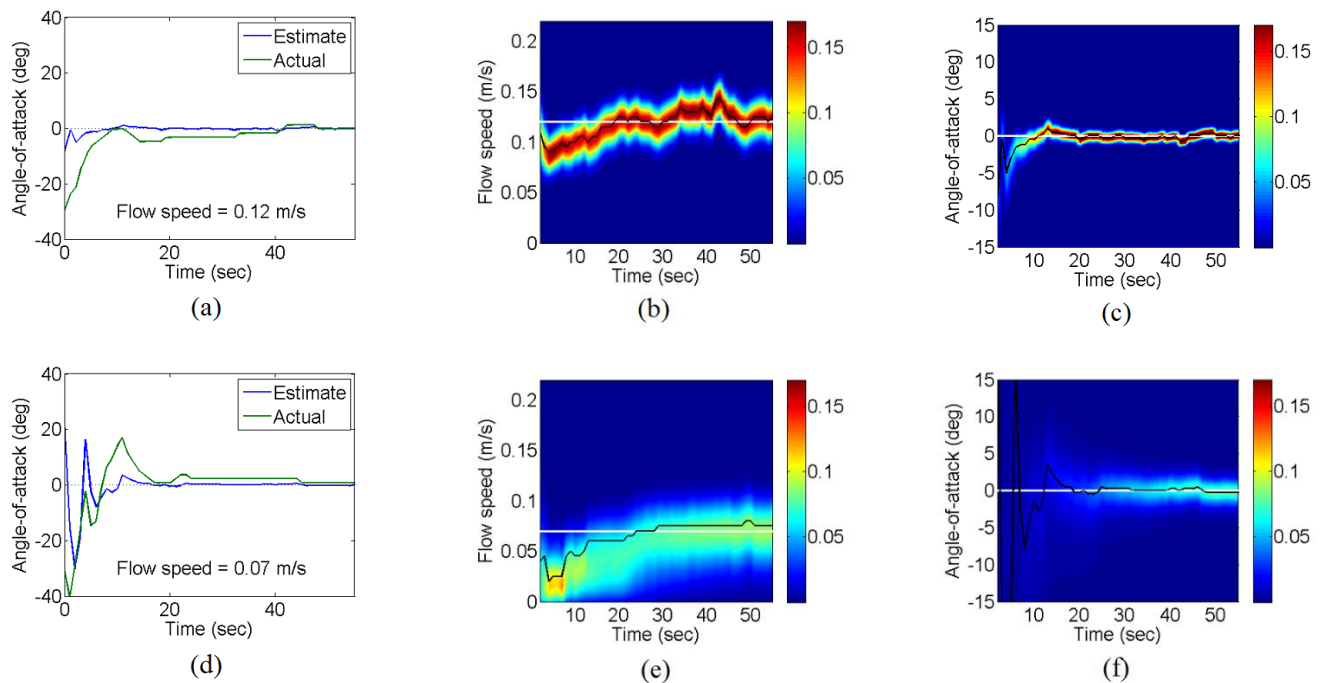
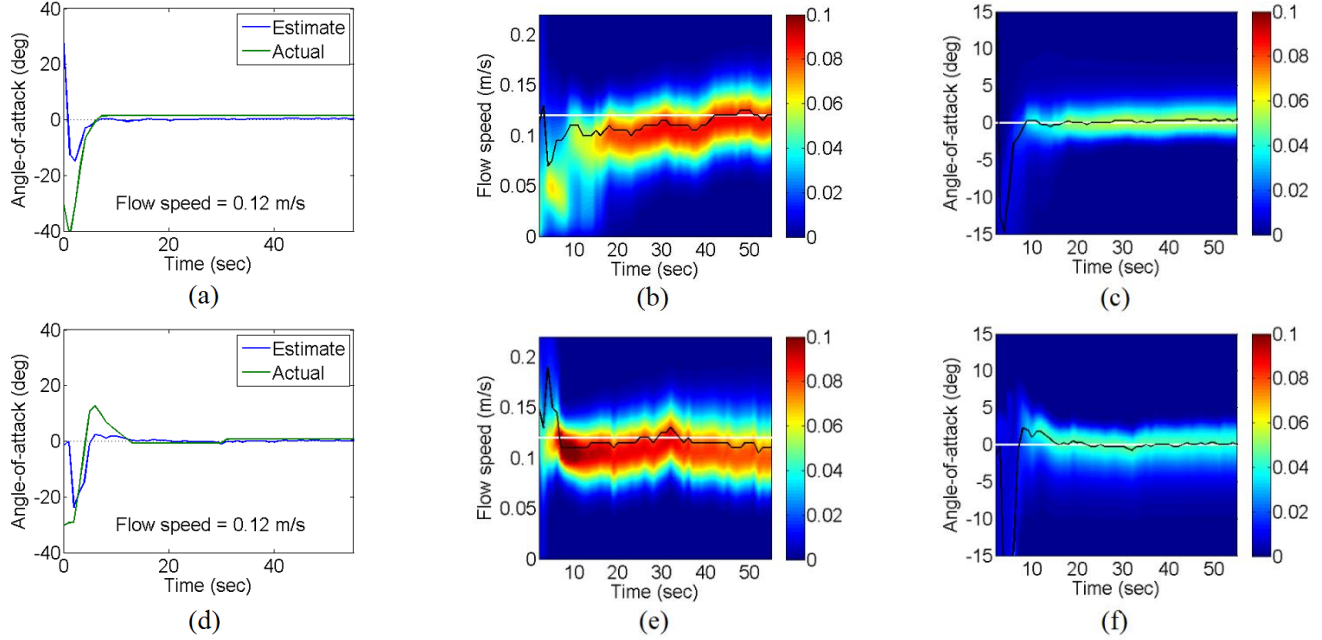


Figure 13 Results from rheotaxis experiments using the Bayesian dynamic feedback controller with the  $[\Delta p_{12}, \Delta p_{13}, \Delta p_{23}]^T$  pressure signals.



**Figure 14** Results from two rheotaxis experiments using the Bayesian dynamic feedback controller with two sensors. (a)-(c) Using the  $\Delta p_{13}$  pressure signal only. (d)-(f) using the  $\Delta p_{23}$  pressure signal only.

One advantage of the simple pressure difference approach is that only two sensors are needed. The results shown thus far for the Bayesian dynamic controller rely on three sensors. To allow further direct comparison to the simple pressure difference approach, we look at the case of only utilizing the  $p_1, p_3$  sensors in the dynamic controller. Note this case represents an example of how the dynamic rheotaxis controller performs if the  $p_2$  nose sensor fails. **Figures 14a-14c** present the results of a rheotaxis experiment using the  $\Delta p_{13}$  signal. The fish robot achieves rheotaxis with a long-term orientation that is robust to noise. **Figures 14d-14f** illustrate the performance of the Bayesian rheotaxis controller in the case of  $p_1$  sensor failure (a sensor on one side of the fish). The fish robot is able to achieve rheotaxis using only the  $\Delta p_{23}$  signal. This result is significant because the  $p_2, p_3$  sensor pair is an asymmetric sensor configuration. We note that both cases of the two-sensor configurations shown here provide accurate estimates of the free-stream flow speed, which was accomplished by modifying the observer process noise variance.

As noted in Section IV, the joint state  $(U, \alpha)$  is not observable for a single sensor pair at a constant angle-of-attack, but observability can be restored if the robot is allowed to move and measurements are integrated in time. Thus, initial conditions with small angle-of-attack resulted in poor estimator performance. Comparing the two-sensor experiments to the three-sensor experiments reveals that properly placed additional sensors can increase the observability of flow field, improving robustness in the estimates and overall estimator performance.

Although empirical methods can be used for rheotaxis behavior in a fish robot, the principled approach outlined here has the following additional advantages: it provides robust rheotaxis performance in the presence of noise; it provides

estimates of both the angle-of-attack and flow speed, which can be used for more complex navigational tasks; it provides extensibility to more sophisticated fluid-mechanical models; it generalizes to asymmetric/arbitrary sensor configurations, requiring only evaluation of the flow model at these sensor locations; and it provides a framework in which information can easily be fused from multiple sensors and multiple sensory modalities.

## VII. CONCLUSION

This work presents a dynamic controller for rheotaxis of a bio-inspired fish robot. The approach employs a fluid-mechanical model for flow around a fish robot based on potential-flow theory and provides estimates of both the fish's orientation and the free-stream flow speed. Experimental results show the dynamic rheotaxis controller reliably achieves rheotaxis despite model error and sensor noise, while providing accurate flowspeed estimates. The estimation-control framework produces a dynamic controller that is less sensitive to noise than a pressure-difference controller and is able to achieve rheotaxis from an initial orientation outside the accurate domain of the potential-flow model. This framework also generalizes to arbitrary sensor placement. The contributions of this paper are significant because rheotaxis and flow speed estimation can be achieved without fitting parameters empirically.

Limitations of this work include the following: a reliance on reduced model error in the zero angle-of-attack orientation, causing reduced performance for orientation control to a non-zero angle-of-attack; and reliance on a relatively uniform flow. In ongoing work, we are considering an extension of this framework to handle non-zero angles of attack and spatially (or temporally) varying flow fields. Improvement of the estimator performance for angle-of-attack through implementation of a

higher fidelity model may enable orientation control to a nonzero angle.

#### ACKNOWLEDGMENT

The authors of this work gratefully acknowledge James Tangorra and Jeff Kahn for lending us the pressure sensors used in this work and Alison Flatau and Steve Day for lending us the flow meter. The authors are also grateful to Cody Karcher, Tom Pillsbury, and Robert Vocke for their mechanical assistance. The authors would also like to acknowledge valuable discussions with Sheryl Coombs, Sean Humbert, Xaiobo Tan, Andrew Lind, and Daigo Shishika. This work is supported by the Office of Naval Research under Grant No. N00014-12-1-0149.

#### REFERENCES

- [1] A. Abdulsadda and X. Tan, "An artificial lateral line system using IPMC sensor arrays," *International Journal of Smart and Nano Materials*, vol. 3, no. 3, pp. 226–242, 2012. [CrossRef](#)
- [2] J. D. Anderson, *Fundamentals of aerodynamics*. New York: McGraw-Hill, 1984.
- [3] M. Asadnia, a. G. P. Kottapalli, Z. Shen, J. M. Miao, G. Barbastathis, and M. S. Triantafyllou, "Flexible, zero-powered, piezoelectric MEMS pressure sensor arrays for fish-like passive underwater sensing in marine vehicles," *2013 IEEE 26<sup>th</sup> International Conference on Micro Electro Mechanical Systems (MEMS)*, pp. 126–129, Jan. 2013. [CrossRef](#)
- [4] N. Beckman, (2013, November 21). "Model Systems in Neuroethology: Prey Capture in Mottled Sculpin." [Online]. Available: [http://nelson.beckman.illinois.edu/courses/neuroethol/models/mottled\\_sculpin/mottled\\_sculpin.html](http://nelson.beckman.illinois.edu/courses/neuroethol/models/mottled_sculpin/mottled_sculpin.html)
- [5] COMSOL, "The CFD module users guide," pp. 1–510, 2012.
- [6] S. Coombs, "Smart skins: information processing by lateral line flow sensors," *Autonomous Robots*, no. 1995, pp. 255–261, 2001. [CrossRef](#)
- [7] S. Coombs, C. B. Braun, and B. Donovan, "The orienting response of Lake Michigan mottled sculpin is mediated by canal neuromasts." *The Journal of Experimental Biology*, vol. 204, no. 2, pp. 337–48, Jan. 2001. [CrossRef](#)
- [8] A. Dagamseh, T. Lammerink, M. Kolster, C. Bruinink, R. Wiegierink, and G. Krijnen, "Dipole-source localization using biomimetic flow-sensor arrays positioned as lateral-line system," *Sensors and Actuators A: Physical*, vol. 162, no. 2, pp. 355–360, Aug. 2010. [CrossRef](#)
- [9] L. DeVries and D. Paley, "Observability-based optimization for flow sensing and control of an underwater vehicle in a uniform flowfield," in *American Controls Conference*, 2013, pp. 1–6. [CrossRef](#)
- [10] R. Fox, A. McDonald, and P. Pritchard, *Introduction to fluid mechanics*, 6th ed. Hoboken N.J.: Wiley, 2004.
- [11] J.-M. P. Franosch, S. Sosnowski, N. K. Chami, K. Kuhlentz, S. Hirche, and J. L. van Hemmen, "Biomimetic lateral-line system for underwater vehicles," *2010 IEEE Sensors*, pp. 2212–2217, Nov. 2010. [CrossRef](#)
- [12] J. Kaipio and E. Somersalo, *Statistical and computational inverse problems*. New York: Springer, 2005.
- [13] A. Klein and H. Bleckmann, "Determination of object position, vortex shedding frequency and flow velocity using artificial lateral line canals." *Beilstein Journal of Nanotechnology*, vol. 2, pp. 276–283, Jan. 2011. [CrossRef](#)
- [14] A. G. P. Kottapalli, M. Asadnia, J. M. Miao, G. Barbastathis, and M. S. Triantafyllou, "A flexible liquid crystal polymer MEMS pressure sensor array for fish-like underwater sensing," *Smart Materials and Structures*, vol. 21, no. 11, p. 115030, Nov. 2012. [CrossRef](#)
- [15] A. Kottapalli, M. Asadnia, J. Miao, C. Tan, G. Barbastathis, and M. Triantafyllou, "Polymer MEMS pressure sensor arrays for fish-like underwater sensing applications," *Micro & Nano Letters*, vol. 7, no. 12, pp. 1189–1192, Dec. 2012. [CrossRef](#)
- [16] A. J. Krener and K. Ide, "Measures of unobservability," in *Proc. of the 48th IEEE Conference on Decision and Control (CDC) held jointly with 2009 28th Chinese Control Conference*. IEEE, Dec. 2009, pp. 6401–6406. [CrossRef](#)
- [17] J. Montgomery, C. Baker, and A. Carton, "The lateral line can mediate rheotaxis in fish." *Nature*, vol. 389, no. 6654, pp. 960–963, Oct. 1997. [CrossRef](#)
- [18] R. L. Panton, *Incompressible flow*. New York: Wiley, 1984.
- [19] C. Peterson and D. A. Paley, "Multivehicle coordination in an estimated time-varying flowfield," *Journal of Guidance, Control, and Dynamics*, vol. 34, no. 1, pp. 177–191, Jan. 2011. [CrossRef](#)
- [20] Z. Ren and K. Mohseni, "A model of the lateral line of fish for vortex sensing." *Bioinspiration & Biomimetics*, vol. 7, no. 036016, pp. 1–14, Sep. 2012. [CrossRef](#)
- [21] Resources Information Standards Committee of British Columbia (2013, November 21). "Field Key to the Freshwater Fishes of British Columbia." Available: <http://www.ilmb.gov.bc.ca/risc/pubs/aquatic/freshfish/fresht-25.htm>
- [22] T. Salumäe and M. Kruusmaa, "Flow-relative control of an underwater robot," *Proc. of the Royal Society A*, vol. 469, no. 20120671, pp. 1–19, 2013. [CrossRef](#)
- [23] T. Salumäe and I. Ranó, "Against the flow: A Braitenberg controller for a fish robot," in *IEEE International Conference on Robotics and Automation*, 2012, pp. 4210–4215. [CrossRef](#)
- [24] J. Tao and X. B. Yu, "Hair flow sensors: from bio-inspiration to bio-mimicking— a review," *Smart Materials and Structures*, vol. 21, no. 113001, pp. 1–23, Nov. 2012. [CrossRef](#)
- [25] R. Venturelli, O. Akanyeti, F. Visentin, J. Ježov, L. D. Chambers, G. Toming, J. Brown, M. Kruusmaa, W. M. Megill, and P. Fiorini, "Hydrodynamic pressure sensing with an artificial lateral line in steady and unsteady flows." *Bioinspiration & Biomimetics*, vol. 7, no. 036004, pp. 1–12, Sep. 2012. [CrossRef](#)
- [26] Y. Yang, J. Chen, J. Engel, S. Pandya, N. Chen, C. Tucker, S. Coombs, D. L. Jones, and C. Liu, "Distant touch hydrodynamic imaging with an artificial lateral line." *Proc. of the National Academy of Sciences of the United States of America*, vol. 103, no. 50, pp. 18 891–5, Dec. 2006. [CrossRef](#)
- [27] Y. Yang, A. Klein, H. Bleckmann, and C. Liu, "Artificial lateral line canal for hydrodynamic detection," *Applied Physics Letters*, vol. 99, no. 2, pp. 023 701–3, 2011. [CrossRef](#)
- [28] Y. Yang, N. Nguyen, N. Chen, M. Lockwood, C. Tucker, H. Hu, H. Bleckmann, C. Liu, and D. L. Jones, "Artificial lateral line with biomimetic neuromasts to emulate fish sensing." *Bioinspiration & Biomimetics*, vol. 5, no. 16001, pp. 1–9, Mar. 2010. [CrossRef](#)